

REPORT DOCUMENTATION PAGE			Form Approved OMB NO. 0704-0188		
<p>The public reporting burden for this collection of information is estimated to average 1 hour per response, including the time for reviewing instructions, searching existing data sources, gathering and maintaining the data needed, and completing and reviewing the collection of information. Send comments regarding this burden estimate or any other aspect of this collection of information, including suggestions for reducing this burden, to Washington Headquarters Services, Directorate for Information Operations and Reports, 1215 Jefferson Davis Highway, Suite 1204, Arlington VA, 22202-4302. Respondents should be aware that notwithstanding any other provision of law, no person shall be subject to any penalty for failing to comply with a collection of information if it does not display a currently valid OMB control number.</p> <p>PLEASE DO NOT RETURN YOUR FORM TO THE ABOVE ADDRESS.</p>					
1. REPORT DATE (DD-MM-YYYY) 01-12-2009		2. REPORT TYPE Final Report		3. DATES COVERED (From - To) -	
4. TITLE AND SUBTITLE Ultra-High Sensitive Magnetoelectric Nanocomposite Current Sensors			5a. CONTRACT NUMBER W911NF-07-1-0435		
			5b. GRANT NUMBER		
			5c. PROGRAM ELEMENT NUMBER 611102		
6. AUTHORS S. Priya, C. Kim, J. Liu			5d. PROJECT NUMBER		
			5e. TASK NUMBER		
			5f. WORK UNIT NUMBER		
7. PERFORMING ORGANIZATION NAMES AND ADDRESSES University of Texas at Arlington Grants and Contracts Services Box 19145 Arlington, TX 76019 -0145			8. PERFORMING ORGANIZATION REPORT NUMBER		
9. SPONSORING/MONITORING AGENCY NAME(S) AND ADDRESS(ES) U.S. Army Research Office P.O. Box 12211 Research Triangle Park, NC 27709-2211			10. SPONSOR/MONITOR'S ACRONYM(S) ARO		
			11. SPONSOR/MONITOR'S REPORT NUMBER(S) 47576-MS.2		
12. DISTRIBUTION AVAILABILITY STATEMENT Approved for Public Release; Distribution Unlimited					
13. SUPPLEMENTARY NOTES The views, opinions and/or findings contained in this report are those of the author(s) and should not be construed as an official Department of the Army position, policy or decision, unless so designated by other documentation.					
14. ABSTRACT Sintered magnetoelectric composites generally exhibit reduced sensitivity due to: 1) breakage and aggregation of ferrite coating during compaction forming path of reduced resistivity, 2) coarsening of piezoelectric particle leading to interfacial porosity, and 3) inter-diffusion between piezoelectric and ferrite resulting in coherency loss. In order to overcome these problems, we are adopting following approach to synthesize core-shell nanocomposites: 1) create piezoelectric particles (sub-micron range) with crystallographic facets which will result in uniform stress					
15. SUBJECT TERMS magnetoelectric, composite, sensor, piezoelectric, magnetostrictive					
16. SECURITY CLASSIFICATION OF:			17. LIMITATION OF ABSTRACT UU	15. NUMBER OF PAGES	19a. NAME OF RESPONSIBLE PERSON Shashank Priya
a. REPORT UU	b. ABSTRACT UU	c. THIS PAGE UU			19b. TELEPHONE NUMBER 540-231-0745

Title: Ultra-High Sensitive Magnetoelectric Nanocomposite Current Sensors

Funding number: W911NF-07-1-0435

Agency report number: 47576-MS

Authors: Shashank Priya, J. Ping Liu, Choongun Kim

- (1) List of papers submitted or published under ARO sponsorship during this reporting period.

Manuscript published in peer-reviewed journals

1. R. A. Islam, V. Bedekar, N. Poudyal, J. P. Liu, and S. Priya, "Magnetoelectric properties of core-shell particulate nanocomposites", J. Appl. Phys. 104 104111 (2008).
2. V. Bedekar, N. Poudyal, C. B. Rong, J. P. Liu, C. Kim, S. Priya "Improved magnetoelectric properties of piezoelectric-magnetostrictive nanocomposites synthesized using high-pressure compaction technique", J. Mater. Sci. 44, 2162-2166 (2009).
3. R. Islam, Y. Ni, A. Khachaturyan, and S. Priya, "Giant magnetoelectric effect in sintered multilayered composite structures", J. Appl. Phys. 104, 044103 (2008).
4. R. A. Islam, C.-b. Rong, J. P. Liu and S. Priya, "Gradient Composite Structure in Cofired Bilayer Magnetoelectric Composites of $\text{Pb}(\text{Zr}_{0.56}\text{Ti}_{0.44})\text{O}_3$ - $\text{Ni}_{0.6}\text{Zn}_{0.2}\text{Cu}_{0.2}\text{Fe}_2\text{O}_4$ System" J. Mater. Sci. Lett. 43, 6337-6343 (2008).
5. R. Islam and S. Priya, "ME Response of Cofired Trilayer Magnetoelectric Composites with Partial Texturing", J. Mater. Sci., (2009) DOI 10.1007/s10853-009-3744-9.
6. R. A. Islam, and S. Priya, "Effect of piezoelectric grain size on magnetoelectric coefficient of $\text{Pb}(\text{Zr}_{0.52}\text{Ti}_{0.48})\text{O}_3$ - $\text{Ni}_{0.8}\text{Zn}_{0.2}\text{Fe}_2\text{O}_4$ particulate composites", J. Mater. Sci. 43, 3560 – 3568 (2008).
7. R. Islam, and S. Priya, "Large magnetoelectric coefficient in Co-fired $\text{Pb}(\text{Zr}_{0.52}\text{Ti}_{0.48})\text{O}_3$ - $\text{Pb}(\text{Zn}_{1/3}\text{Nb}_{2/3})\text{O}_3$ - $\text{Ni}_{0.6}\text{Cu}_{0.2}\text{Zn}_{0.2}\text{Fe}_2\text{O}_4$ trilayer magnetoelectric composites", J. Mater. Sci. 43, 2072 – 2076 (2008).

8. R. A. Islam, D. Viehland, and S. Priya, "Doping effect on magnetoelectric coefficient of $\text{Pb}(\text{Zr}_{0.52}\text{Ti}_{0.48})\text{O}_3\text{-Ni}_{(1-x)}\text{Zn}_x\text{Fe}_2\text{O}_4$ particulate composite", *J. Mater. Sci.* 43, 1497 – 1500 (2008).
9. R. Islam and S. Priya, "ME Response of Cofired Trilayer Magnetoelectric Composites with Partial Texturing", *J. Mater. Sci.*, (2009) (accepted).

Manuscript accepted for publication

1. V. Bedekar, R. Islam, H. Kim, M. I. Bichurin, S. N. Ivanov, Y. J. Pukinski and S. Priya, "Magnetoelectric Gradiometer", *European Physical Journal B*, Aug. 2009.
2. V. Bedekar, G. Singh, R. Mahajan and S. Priya, "Synthesis and Microstructural Characterization of Barium Titanate Nanoparticles Decorated SiCN-MWCNT Nanotubes – "nanoNecklace", *Ferroelectrics*, 2009.

Papers presented at meetings, but not published in conference proceedings

1. V. Bedekar, M. I. Bichurin, S. N. Ivanov, Y. J. Pukinski, H. Kim, R. A. Islam, and S. Priya, "Magnetoelectric Gradiometer", MEIPIC6 workshop 2009.
2. C. Park, H. Kim, R. Mahajan, S. Priya, "Multilayer Magnetoelectric Nanostructures of $\text{CoFe}_2\text{O}_4\text{ – BaTiO}_3$ ", *MS&T'08 (October 5 – 9, 2008, David L. Lawrence Convention Center, Pittsburg, PA)*
3. R. Islam, N. Podual, J. P. Liu, C. Kim, S. Priya, "Synthesis of Layered Magnetoelectric Composites through "Bottom-Up" Approach", *MS&T'08 (October 5 – 9, 2008, David L. Lawrence Convention Center, Pittsburg, PA)*
4. Invited talk, S. Priya, Magnetoelectric Composites, 2009 MRS Spring Meeting, San Francisco, CA, April 13 – 17 (Symposia I: Multiferroics and Magnetoelectrics).
5. Invited presentation, S. Priya, "Structure - property relationships in perovskite - spinel based magnetoelectric composites", The Rank Prize Funds Mini-Symposium on Periodically-Modulated and Artificially Hetero-Structured Devices Wordsworth Hotel, Grasmere, Cumbria LA22 9SW, UK, 18th to 21st May 2009.

6. R. A. Islam, and S. Priya, "Grain Size dependence of magnetoelectric coefficient in $\text{Pb}(\text{Zr}_{0.52}\text{Ti}_{0.48})\text{O}_3 - 0.2\text{Ni}_{0.8}\text{Zn}_{0.2}\text{Fe}_2\text{O}_4$ System", 109th Annual Meeting of The American Ceramic Society combined with MS&T'07, September 16 – 20, Detroit, MI, (2007).
7. R. B. Mahajan, H. Kim, R. Islam, M. Karmakar, and S. Priya, "Multilayer magnetoelectric nanostructures of $\text{CoFe}_2\text{O}_4 - \text{BaTiO}_3$ ", 109th Annual Meeting of The American Ceramic Society combined with MS&T'07, September 16 – 20, Detroit, MI, (2007).

(2) Demographic data for this reporting period

1. Number of manuscript submitted during this reporting period – 0
2. Number of peer-reviewed papers submitted during this reporting period – 9
3. Number of Non-peer reviewed papers submitted during this reporting period – 0
4. Number of presented but not published papers submitted during this reporting period – 7

(3) Demographic Data for the life of this agreement:

1. Number of PhD(s) awarded as a result of this agreement – 1
2. Number of Grad Students supported by this agreement – 2.0
3. Number of post doctorates supported by this agreement – 0.5
4. Number of faculty supported by this agreement – 3

Scientific progress and accomplishments

(A) **Synthesis of NiFe_2O_4 nanoparticles** (J.P. Liu and N. Poudyal, Department of Physics, University of Texas-Arlington): The synthesis was performed with standard airless chemical synthesis technique in a nitrogen atmosphere. The reagents were obtained from commercial sources and used without further purification. In a typical synthesis of 18 nm NiFe_2O_4 nanoparticles a mixture of 257 mg of $\text{Ni}(\text{acac})_2$, 500 mg of 1,2- hexadecanediol was added to a 125 mL European flask containing a magnetic stir bar. Benzyl ether 20 mL was then transferred into the flask and the contents were stirred while purging with N_2 for 20 minutes at room temperature. The flask was then heated to 120 °C and the temperature was held for 20 minutes. During this time, 0.2 ml of $\text{Fe}(\text{CO})_5$ was injected into the flask while the N_2 purge continued. After 3 minutes, 1 mL of oleic acid and 1 mL of oleyl amine were injected and the mixture was maintained under N_2 blanket and heated to 160 °C at a rate of 5 °C per minute was held for 10 minutes. The flask was maintained at the refluxing temperature of 295 °C for 30 minutes before cooling down to room temperature under the N_2 blanket. Afterwards, all handling was

performed open to the atmosphere. The as-synthesized black product was precipitated when adding ethanol and separated by centrifugation at 6000 RPM for 20 minutes. The supernatant was discarded and the precipitate was re-dispersed in 10 mL of hexane and 30 mL of ethanol for further purification. This dispersion was centrifuged for 15 minutes at 6000 RPM. The supernatant was discarded and the remaining dark brown precipitate was redispersed in hexane and stored under refrigeration.

Size of NiFe_2O_4 nanoparticles were controlled well by varying solvent, amount of surfactants and heating rates. For example, when benzyl ether was replaced by phenyl ether, particles size were reduced from 18 nm to 6 nm keeping other reaction parameters same. But when benzyl ether was used as solvent and amount of both the surfactants were increased from 1 ml to 2 ml the size particles were increased from 18 nm 22 nm. X-ray diffraction patterns, TEM images and hysteresis loops of as-synthesized NiFe_2O_4 nanoparticles are shown below in Fig.'s (1-3).

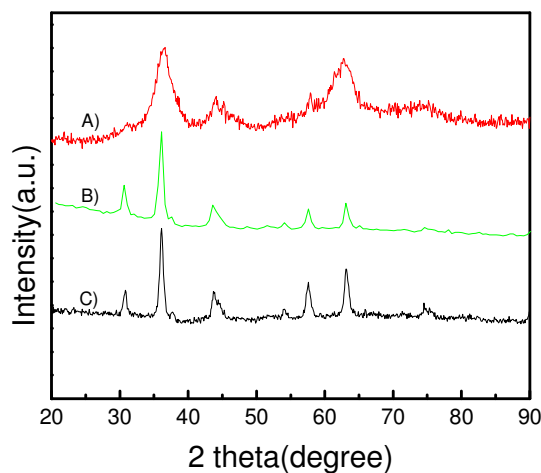


Figure 1: X-ray diffraction patterns of NiFe_2O_4 nanoparticles (a) 6 nm, (b) 18 nm, and (c) 22 nm.

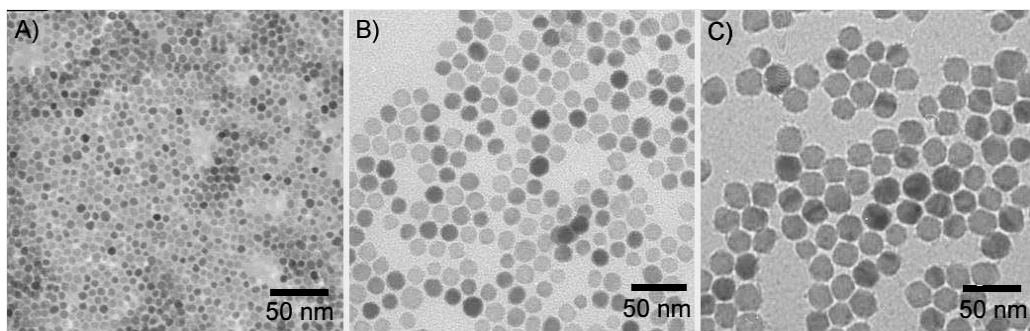


Figure 2: TEM images of NiFe_2O_4 nanoparticles (a) 6 nm (b) 18 nm and (c) 22 nm.

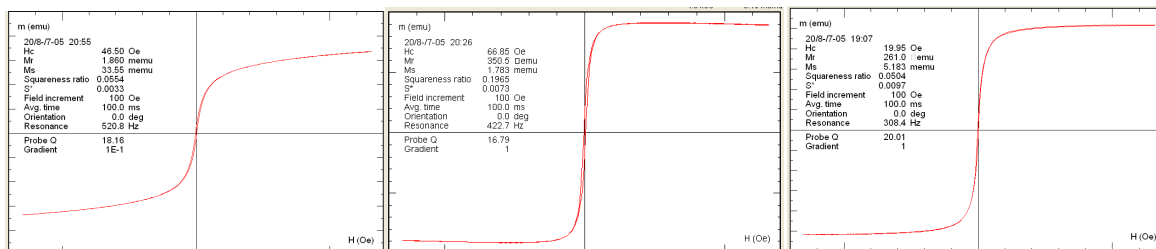


Figure 3: Hysteresis loops of NiFe₂O₄ nanoparticles (a) 6 nm (b) 18 nm and (c) 22 nm.

(B) Coating of NiFe₂O₄ on PZT (J.P. Liu and N. Poudyal, Department of Physics, University of Texas-Arlington): Coating experiments of NiFe₂O₄ nanoparticles on PZT particles were performed by chemical synthesis method following the similar recipes used for synthesis of NiFe₂O₄ nanoparticles with addition of PZT particles as seeds to be coated. In a typical coating experiment of NiFe₂O₄ on PZT particles a mixture of 257 mg of Ni(acac)₂, 280 mg of 1,2- hexadecanediol and 2 gram of PZT was added to a 250 mL European flask containing a magnetic stir bar. Benzyl ether 25 mL was then transferred into the flask and the contents were stirred while purging with N₂ for 20 minutes at room temperature. The flask was then heated to 120 °C and the temperature was held for 20 minutes. During this time, 0.2 ml of Fe(CO)₅ was injected into the flask while the N₂ purge continued. At 140 °C, 1 mL of oleic acid and 1 mL of oleyl amine were injected and the mixture was maintained under N₂ blanket and heated to 160 °C at a rate of 5 °C per minute was held for 10 minutes. The flask was maintained at the refluxing temperature of 295 °C for 30 minutes before cooling down to room temperature under the N₂ blanket. Purification coated samples was done following similar process to NiFe₂O₄ nanoparticles mentioned above. Coating experiments were done on different compositions of PZT seeds particles and also varying the initial precursor's weight ratios of NiFe₂O₄ and PZT particles.

Composition of PZT particles used for coating are as following:

- PZT_(0.80)PZN_(0.20)
- PZT_(0.85)PZN_(0.15)
- PZT_(0.80)PZN_(0.20)+0.5 % CuO
- PZT_(0.95)PZN_(0.05)+ 0.9% Mn

Initial precursor weight ratios of NiFe₂O₄ and PZT seeds particles were varied from 1, 2 and 3 folds.

(C) Synthesis of core-shell composite structure using conventional sintering (R. Islam, and S. Priya, Materials Science and Engineering, University of Texas-Arlington): Figure 4(a) shows the SEM images of PZT – NF core shell structure. EDS spot analysis on these particles showed presence of both PZT and NF. Figure 4(b) shows the TEM image of PZT particle coated with NF nano particles. The difference in contrast was clearly observed for two different sizes of particles. TEM investigations showed that the NF nanoparticle shell over the PZT core was 2-3 layers in thickness. Figure 4(c) shows the low magnification SEM image of PZT – NF core-shell structure. The microstructure of the sintered composite was dense with very small fraction of porosity. The grain size of the composite was found to be in the range of 500–800 nm. Inset of Fig. 4(c) shows a magnified view of core-shell grains. TEM analysis revealed that the shell was present at the grain boundary of large fraction of grains. The coating thickness was equivalent to 2 – 3 layers, which varies from 40–70 nm. The size of nanoparticles in the shell was larger than the as-synthesized nanoparticles due to high temperature sintering process. Figure 2(d) shows the magnetic properties of as synthesized NF nanoparticles and PZT – NF

core-shell structure. One major difference can be immediately noted in this figure related to increase in coercive field as compared to the nanoparticles. For PZT – NF core-shell particles the coercive field was found to be 216 Oe whereas for as synthesized nanoparticles this magnitude was significantly lower. This may be attributed to the increase in size of NFO shell during sintering process. As particle size decreases, coercivity decreases and for very low value of particle size ferromagnetic to super-paramagnetic transition occurs. It has been shown in literature that with increasing particle size from 1 nm and above, the magnitude of coercive field increases and reaches maxima before dropping again with further increase in size. The particle size where maximum in coercive field occurs corresponds to the size of single domain particle. The size of shell in the sintered composite may be close to the single domain particle size and hence the coercive field observed was high.

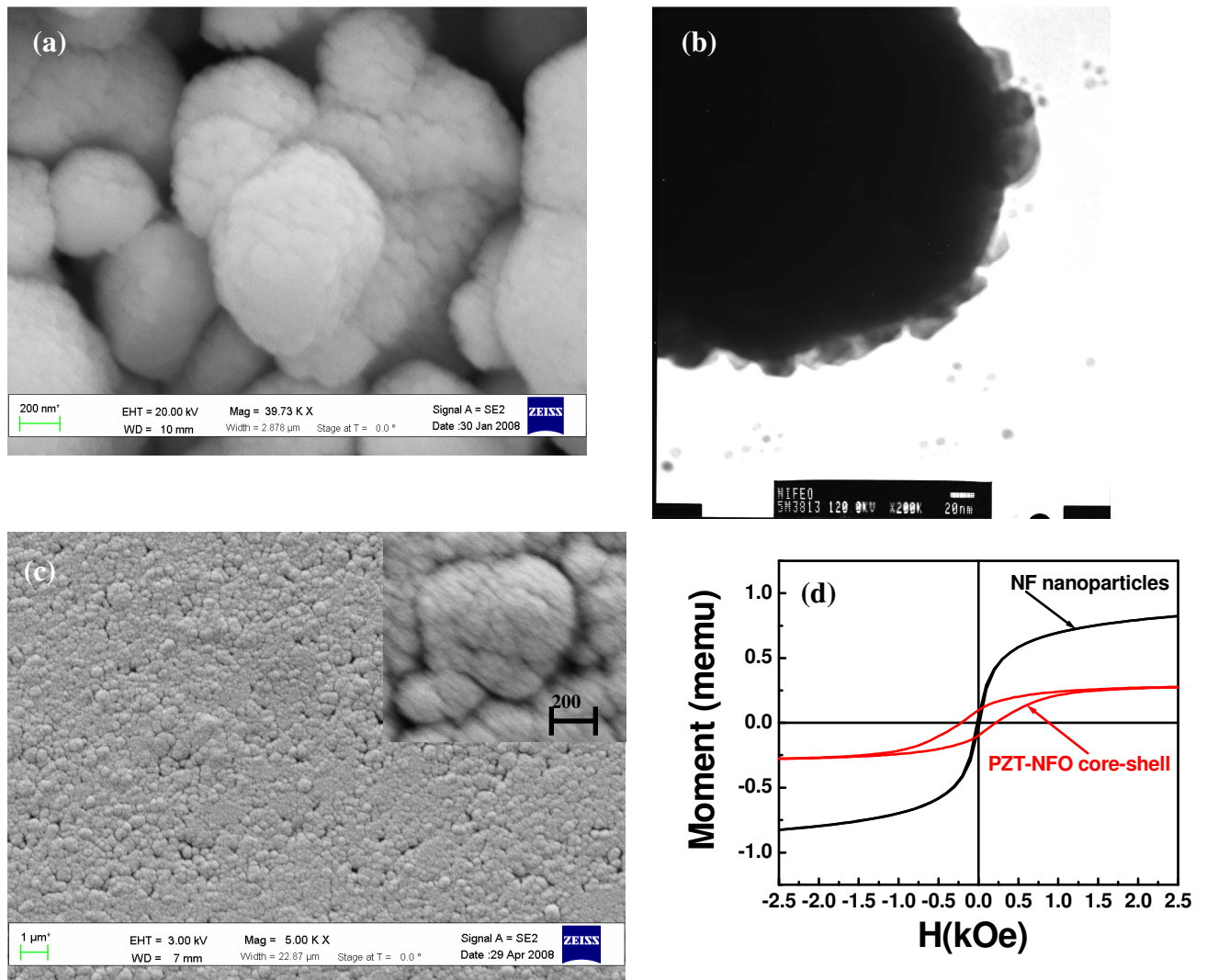


Figure 4: Micrographs for PZT – NF core-shell structure, (a) SEM and (b) TEM, (c) SEM microstructure of sintered PZT – NF core shell structure, and (d) comparison of magnetic hysteresis property of NF nano particles and PZT – NF core – shell structure.

Figure 5(a) shows the TEM microstructure of sintered composite and Fig. 5(b) shows the variation of magnetoelectric coefficient as a function of DC bias. The piezoelectric (d_{33}) and dielectric properties were measured on aged samples. The composite had d_{33} of 60 pC/N, dielectric constant of 865 and dielectric loss of 5.45%. The peak ME coefficient of 195 mV/cm.Oe was observed at 454 Oe. This magnitude is much higher than that obtained for random polycrystalline sintered composites and about 130 times higher than that reported for the BaTiO₃-CoFe₂O₄ core-shell composites.

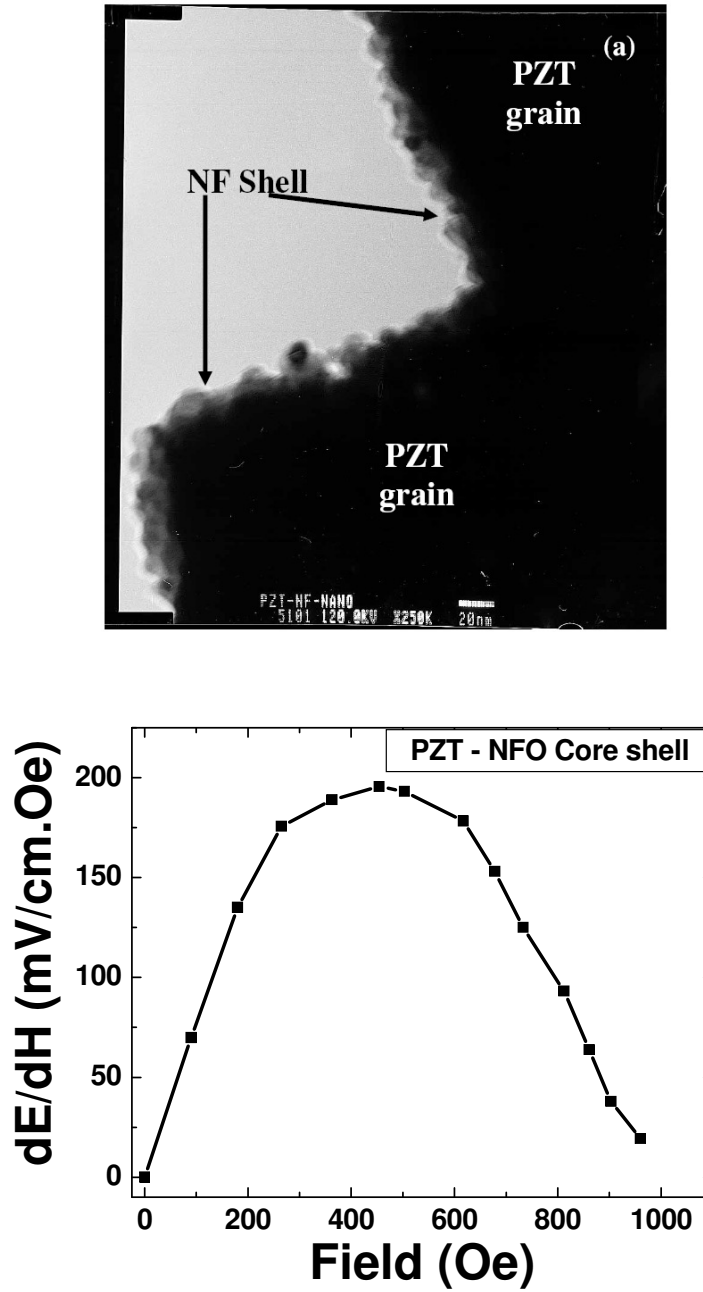


Figure 5: (a) TEM image of sintered composite and (b) magnetoelectric coefficient as a function of DC bias field for sintered PZT – NF core shell structure.

(D) High Pressure Compaction of NiFe_2O_4 -coated PZT particles (J.P. Liu, N. Poudyal, V. Bedekar, S. Priya, and C. Kim Department of Physics, University of Texas-Arlington): High-pressure sintering was conducted to achieve homogenous microstructure with ordered distribution of NFO phase. PZT–NFO composite particles were pressed using a 0.25-in. disc-shaped die at 2 kpsi and sintered at 1 GPa and 600°C for 30 min using Rockland SV-TC high compaction machine. After sintering, the bi-layer sample was removed from the metal die using a coarse file. The thickness of PZT–NFO layer in this bi-layer composite was 0.2 mm. The sample was then annealed at 1040°C for 3 h, electroded, and, subsequently, poled at 2.5 kV/mm in silicon oil bath at 120°C for 30 min. piezoelectric dielectric properties were measured using conventional techniques.

Figure 6(a) and (b) shows the TEM bright-field (BF) and dark field (DF) image of PZT–NFO-sintered composite. The contrast clearly shows the presence of NFO phase (dark spots at BF) on the bigger PZT grains. SAED pattern indicates the presence of NFO (111) phase with some arc formation in the ring diffraction pattern. The arcs suggest minor texturing effect of NFO phase for some of the grains in the area under investigation. These NFO fragments are fully crystallized after the sintering and annealing process. Based upon the TEM analysis, the microstructure of the composite is schematically depicted in Fig. 6(c). The microstructure reveals well-grown PZT grains with NFO clusters dispersed along the initial grain boundary formed during high-pressure compaction. These NFO clusters migrate from the initial location resulting in mixed orientation of NFO phase at the initial grain boundaries of PZT grains as well as randomly dispersed NFO islands on PZT grains. In conventional particulate-sintered composites consisting of magnetostrictive and piezoelectric grains, the interfacial defects are distributed throughout the microstructure resulting in porosity and heterogeneity. This drawback can be overcome by synthesizing the microstructure shown in Fig. 6. In addition, the ordered distribution of NFO phase will preserve the physical properties of piezoelectric and magnetostrictive phase. In particulate-sintered composites consisting of random distribution of magnetostrictive particles, there is excessive cross-diffusion of ions across the interface. Recently, it was shown in Cu-modified nickel zinc ferrite (NCZF)–PZNT composites that Cu ions diffuse into PZNT while Pb ions diffuse into NCZF. Another drawback for particulate-sintered composites is connectivity between ferrite particles lowering the resistivity of the sample and making it difficult to pole. By confining the distribution of NFO along grain boundaries and controlling fraction of such boundaries can result in applying higher poling voltage.

The peak ME coefficient of 187 mV/cm.Oe was found at 285 Oe DC bias field. The results showed that high pressure compaction results in enhanced ME coefficient compared to the conventionally sintered samples but the magnitude is still not high enough to meet the sensing requirements. This enhancement was correlated to the partially disordered and ordered orientation and distribution of NFO particles along the PZT grains. The piezoelectric grains in this microstructure are under compressive strain due to the difference in volume of unit cell between spinel and perovskite phase. This strain will be accommodated by defect formation at the grain boundary and shape changes leading to gradient from the boundary towards the center of the grain. The presence of gradient strain due to lattice mismatch will assist the deformation of piezoelectric grains under magnetostrictive stress due to systematic variation in

magnitude of mechanical impedance. A detailed TEM analysis was conducted to verify these predictions and the result helped us in further improving our design of nanocomposite.

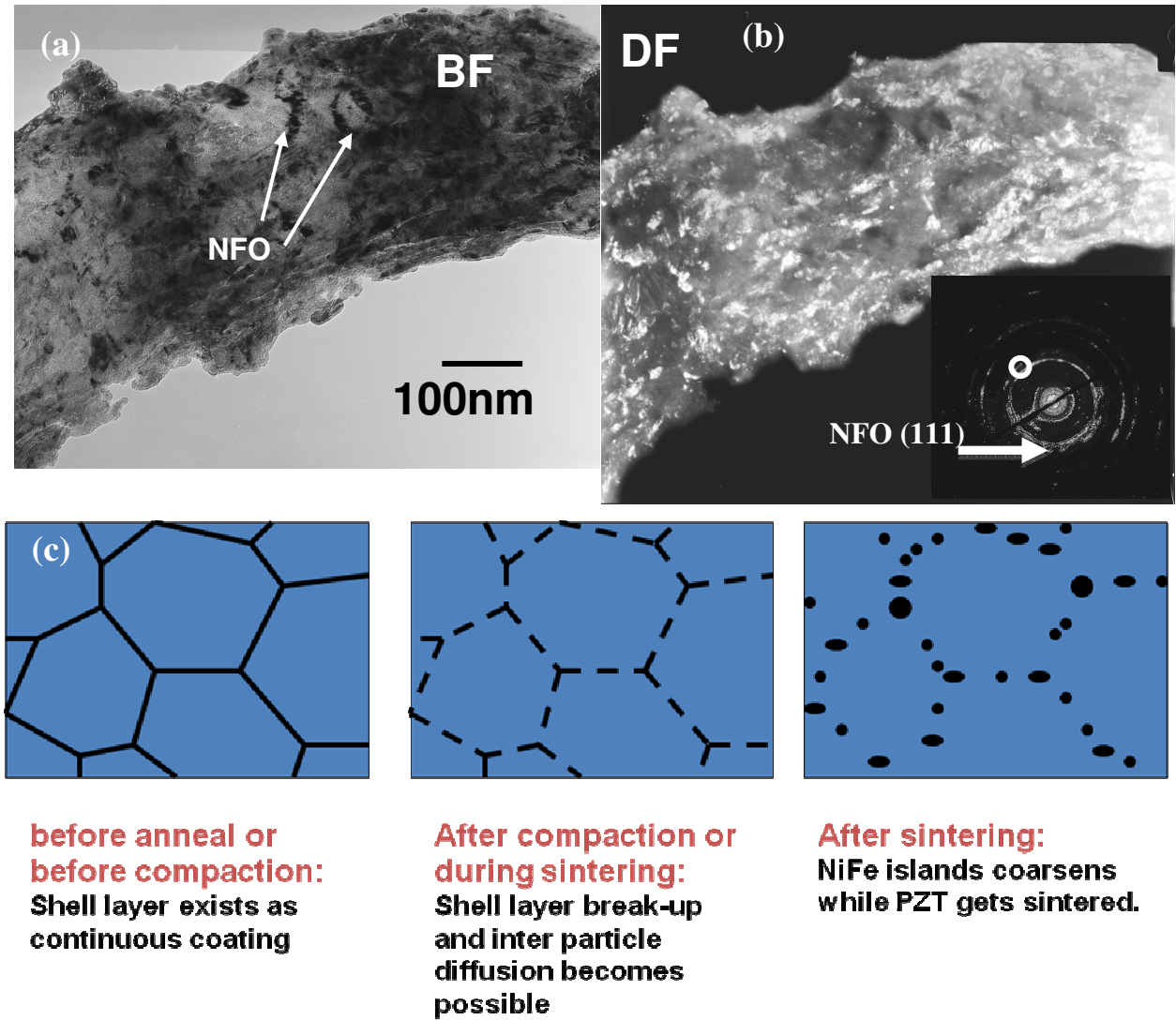


Figure 6: TEM analysis of the high-pressure compacted nanocomposite. (a) Bright-field image. (b) Dark-field image. (c) Schematic illustration of the microstructure under high – pressure compaction. The dark-field image is taken from the NFO (111) diffraction spot (circled area) and, therefore, not all NFO phases is visible as white contrast.

(E) Textured layered-magnetoelectric composites (R. Islam, and S. Priya, Materials Science and Engineering, University of Texas-Arlington): Crystallographic texturing of piezoelectric phase can improve the piezoelectric and ferroelectric response by exploiting the anisotropy of electrical properties. The goal of this study was to utilize the texturing process in heterogeneous system consisting of varying crystal structure. This will allow developing core-shell composite materials that exhibit maximum response. As a simple rule, the rhombohedral phase oriented along the $\langle 100 \rangle$ direction provides higher

piezoelectric response. Texturing can be accomplished through various processes including, hot pressing (HP), templated grain growth (TGG) and reactive template grain growth (RTGG). The advantage of TGG over HP is that the process is conducted using steps similar to that of conventional ceramic processing except with added seed material. In HP, there is a possibility of abnormal grain growth along the pressing direction. Hence in this study, the TGG technique was adopted to synthesize the textured composites. The texturing process consists of two important steps: (i) seed fabrication, and (ii) seed alignment in the matrix.

To fabricate the seed (template), molten salt synthesis technique was followed. It is desirable to have the seed crystal of same crystal structure as that of matrix. In this respect, BaTiO_3 was chosen as the seed material since it can be grown in large size using Remeika process. This synthesis process consists of heating the raw materials (BTO covered with KF salt in Pt crucible) at 1150 to 1225°C for 8-12 hours and then slowly cooling down to the room temperature. The crystals were separated from KF salt by hot water. The size of synthesized BaTiO_3 seed was found to be in the range of 75 – 200 μm . Some seeds were found to be as large as 2 – 3 mm plates. Figure 7(a) shows the optical image of the BTO seed fabricated using Remeika method. There were facets observed at the surface of the seed which could be related to the twins. A high magnification optical image (inset) shows these facets of single crystal cover the whole surface. X-ray diffraction pattern of the seeds in Fig. 7(b) shows strong intensity peak near 22.2° which is (001) peak of the perovskite BTO.

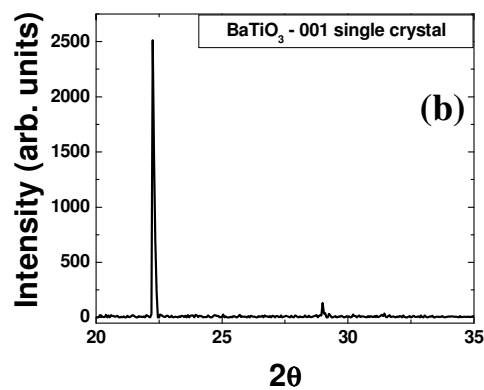
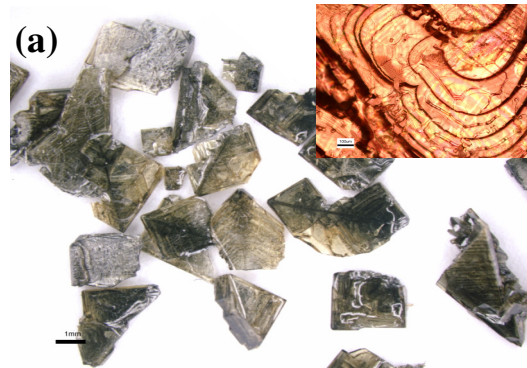


Figure 7: (a) Optical images of large size BTO seed crystal, (inset: facets or growth marks) (b) X-ray diffraction pattern of BTO seed showing (001) orientation.

The seed crystals were used as templates for texturing piezoelectric phase in the trilayer ME composite. For this purpose, small amount (1 – 5 wt. %) of seed was mixed with the piezoelectric powder (e.g. PZT – PZN). Trilayer was pressed using NCZF top and bottom layer with seeded PZT – 15% PZN in the middle. The sample was kept for sintering in an air atmosphere for 50 hr soaking time so that the grains can grow along the orientation of the seed crystal. A bilayer sample was also synthesized in order to study the structural characteristics of PZT layer.

From X-ray diffraction patterns the degree of texturing was calculated by Lotgering method. Lotgering factor is defined as the ratio of area textured along the crystallographic plane of interest given as:

$$f_{00l} = \frac{P_{00l} - P_0}{1 - P_0}, \text{ where } P_{00l} = \frac{\sum I_{00l}}{\sum I_{hkl}} \text{ and } P_0 = \frac{\sum I_{00l}^0}{\sum I_{hkl}^0}$$

where I_{hkl} and I_{hkl}^0 are the intensities of hkl plane for the textured and random sample and $\sum I_{00l}$ is the summation of the intensities of all 001 planes (001, 002 etc.). The Lotgering factor was calculated to be $f = 0.35$ for samples textured along $\langle 001 \rangle$ direction. The textured grain size observed was in the range of 200 – 350 μm compared to 1 – 2 μm size for randomly oriented grains. The grain size observed is very high due to large soaking period of 50 hrs which also helps to orient the grains. Small size seeds were observed near the textured grains. In the sintered composite, PZT-PZN layer was found to be around 0.5 mm in thickness and NCZF thickness was of the order of 1.2mm. The samples were poled at 120°C for 20 minutes under a field of 2.5 kV/mm in a silicone oil bath. The longitudinal piezoelectric constant (d_{33}) was measured to be 325 pC/N, with dielectric constant of 1865 and loss of 7% at room temperature at 1 kHz. Compared to the random PZT – PZN intermediate layer, d_{33} increases by 44% and dielectric constant increases by 50% for the moderate degree of texturing. Figure 8 shows the ME coefficient of trilayer with textured PZT – PZN as function of DC bias. The peak ME coefficient observed was around 878 mV/cm.Oe at 300Oe DC bias field. For the same thickness of randomly oriented grains, ME coefficient observed was around 526 mV/cm.Oe. This increase in piezoelectric and magnetoelectric coefficient in the textured trilayer can be explained as the increased spontaneous polarizations due to increased grain orientation along $\langle 001 \rangle$ direction. During poling as the field is increased, the domain rotation takes place along $\langle 001 \rangle$ from any of the four equivalent $\langle 111 \rangle$ directions, which increases the strains.

The results of this experiment are very exciting and lead us to the conclusion that textured layered composite from core-shell particles may provide enhancement in the magnetoelectric performance. We have just started tape-casting experiments to further investigate this direction. Currently, we are optimizing the slurry composition and sintering behavior. Once that is done, we will start to conduct the texturing experiments on layers in the range of 50 – 100 μm . The textured laminates will be applied for the broadband sensor being developed in this program.

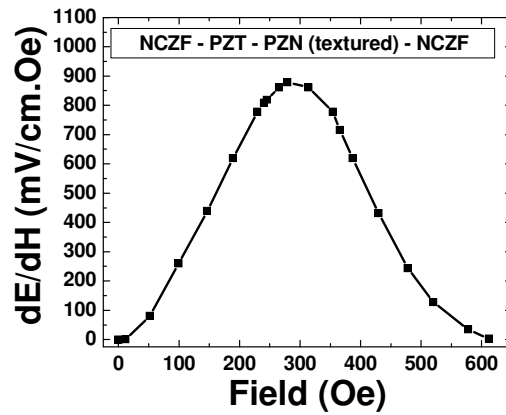


Figure 8: ME coefficient of the textured ME composite.

(F) Synthesis and Microstructural Characterization of Barium Titanate Nanoparticles Decorated SiCN-MWCNT Nanotubes – “nanoNecklace”

Experiments were conducted on the synthesis and characterization of flexible polymer-derived ceramic silicon carbon nitride nanotubes decorated with barium titanate (BTO) nanoparticles with multi-walled carbon nanotubes acting as a template. The synthesis was achieved by controlled pyrolysis of polyurea (methylvinyl) silazane and BTO metal-organic precursor. Structural characterization was conducted by advanced microscopy techniques revealing 10 – 50 nm BTO nanoparticles uniformly covering the SiCN coated CNT nanotubes. X-ray photoelectron spectroscopy was used to confirm the BTO perovskite phase. Possible application of this novel structure—nanoNecklace – is in building ultra sensitive ME sensors and also capacitors. We were successful in synthesizing periodic arrangement of BTO nanoparticles on the SiCN surface using MWCNT as template. Since the architecture of this nanostructure resembles that of a “necklace”-, BTO pearls assembled around the SiCN-MWCNT string- we have named this novel structure as “nanoNecklace”. This is one possible arrangement of BTO at nanoscale. Polymer derived ceramic, SiCN, is a unique material, which depending upon the processing conditions, can possess electrical properties ranging from those of a complete insulator to a near electrical conductor. This material has also been demonstrated as a heat dissipating material which could be an attractive property when driven at high electric fields. Flexibility of the SiCN-MWCNTs structure allows easy manipulation and positioning on a given substrate. In addition, SiCN layer modifies the surface wetting characteristics of MWCNTs thereby promoting the adhesion of BTO nanoparticles.

Size effect is an important consideration in ferroelectrics. Studies on BTO have shown that the minimum grain dimensions that maintain ferroelectricity are 50nm for pure ceramics and 110 nm for the doped. Theoretical models also predict the critical size for pure BTO to be 44nm. Further it has been found that pure BTO has slightly smaller tetragonality in the powder form (as compared to single crystal) and the doped ceramics have much smaller tetragonality than of the pure ceramics. The reasons for these effects

have been attributed to the intrinsic lattice stress. SEM analysis combined with the surface tension measurements indicate that the surface bond contraction due to small size induces a compressive stress on the inner part of a grain. This effect plays an important role in ferroelectric materials in the nanometer size range. The induced stress causes decrease of Curie temperature and spontaneous polarization: with decreasing grain size, both of these effects get magnified. Another size- driven effect is the dielectric anomaly that arises due to the surface bond contraction. The domain wall contribution has an opposite effect compared to that with the surface bond contraction induced effect. When the grain size decreases to a value comparable to the width of domain walls, pinning points develop inside the grains and the domain wall motion is inhibited. The reduced wall mobility causes a decrease in the relative permittivity. The net effect depends on the relative play of the increase of relative permittivity by the surface bond contraction effect and its decrease by the domain wall pinning effect. These considerations are important for designing the nanostructures since if the grain size is smaller than the critical size, then the residual internal stress in the ceramic may lead to decrement in the permittivity. The decrement in permittivity is rapid beyond the critical size. Thus, our goal was to achieve BTO particle dimensions in range of 20 – 50 nm which is challenging as smaller sizes are preferable for coating.

BTO- decorated SiCN nanotubes were synthesized by pyrolysis of polyurea (methylvinyl) silazane (CerasetTM Kion Specialty Polymers, Charlotte, NC) and barium titanium ethylhexano-isopropoxide metal-organic precursor on the surfaces of MWCNTs. Commercially available liquid Ceraset and barium titanium ethylhexano-isopropoxide (Alfa AesarTM) were used as precursors for SiCN and barium titanate respectively. MWCNTs were used as a template material for SiCN monolayer coating. The first step in synthesis was wetting of nanotubes with Ceraset by addition of 50 vol% of CNTs in a 5 vol% solution consisting of Ceraset and ethanol. This solution was ultra-sonicated for 30 min resulting in uniform coating of nanotubes with Ceraset. The second step consisted of adding 10vol% of BTO precursor to Ceraset-CNT solution followed by ultrasonication for 1 hr. The solution was then dried in air at ~80°C under magnetic stirring to allow evaporation of ethanol. Dried powder was then cross-linked and pyrolyzed in an alumina tube furnace using two-step annealing profile under high purity nitrogen atmosphere. The annealing process consisted of heating the powder to 400°C and holding for 2 hrs (for cross-linking of the Ceraset polymer), followed by heating at 900°C for 4 hrs (to convert polymer into ceramic).

Figure 9(a) and (b) show the microstructure of BTO coated on SiCN-MWCNTs. The nanotubes were found to have the diameter of 20 to 100 nm while BTO nanoparticles were found to be in the range of 10 ~ 40 nm in size. It was found that the nanotubes with larger diameter were fully coated with BTO nanoparticles while those with diameter in the range of 20 ~ 40 nm were only partially coated. This indicates that there is a specific size ratio ($r_{\text{MWCNT}}/r_{\text{BTO}}$) beyond which adhesion between the two phases (BTO and SiCN) becomes stronger due to increased surface area. We also expect that the wetting characteristics play an important role in achieving the adhesion between SiCN and BTO. Nanotubes with larger diameters contain higher number of surface defects providing smaller liquid contact angles as compared to thinner nanotubes. Barber et al. have experimentally shown that wetting properties are dependent upon the diameter (or curvature) of MWCNTs and the wetting properties are different for internal and external

surfaces. A monolayer coating of SiCN on the surface of MWCNTs increases the surface roughness and promotes wetting. SEM elemental mapping analysis (BrukerTM EDX with a Silicon Drifted Detector) revealed presence of barium and titanium on the surface of the sample as shown in Fig. 9(b). Corresponding elemental spectra are shown in Fig. 9(c).

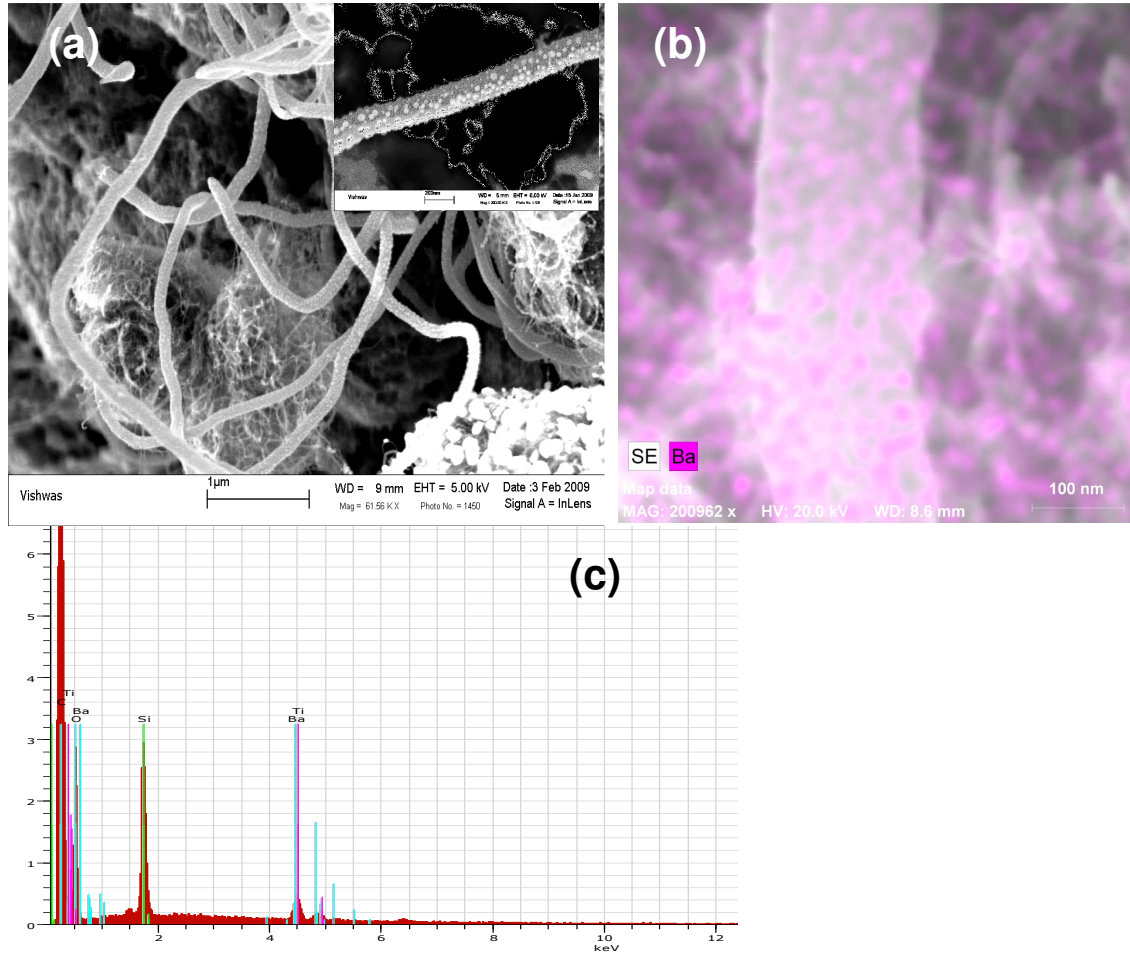


Figure 9: (a) FE-SEM image showing BTO nanoparticles covering the nanotube surface. Inset shows high magnification image of the area corresponding to nanotube surface; (b) EDS- elemental map corresponding to Ba element, showing the presence of barium in the nanoparticles and (c) EDS- spectra corresponding to Fig. 9(b).

HRTEM analysis was conducted to confirm the presence of BTO nanoparticles (200 keV, FEI Company Titan 300). Figure 10(a) and (b) show the TEM images of synthesized nanoNecklace. The bright field image shows the presence of BTO nanoparticles with a clear contrast in high angle annular dark field (HAADF) image indicating coating of BTO on larger diameter nanotubes. Figure 10(c) and (d) show the HAADF high magnification micrographs of individual nanoNecklace with contrast in distribution of BTO phase and underlying SiCN phase. HAADF – EDS analysis confirmed the presence of Ba, Ti, Si, O and C elements as shown in the spectrum.

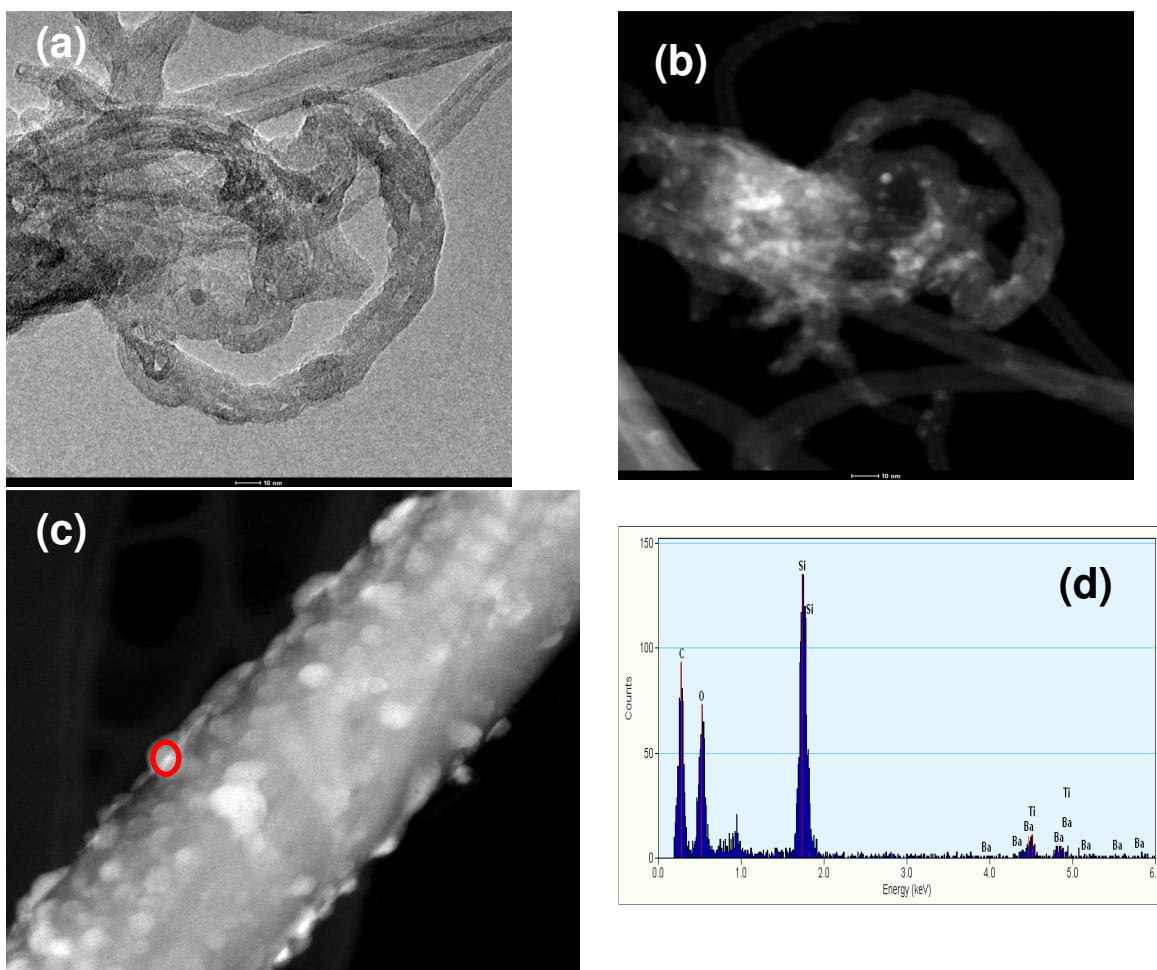


Figure 10: Scanning TEM images of NTs covered with BTO particles (a) Bright Field (BF) image (b) High Angle Annular Dark Field (HAADF) image (c) HAADF image of a single NT. Heavy elements such as Ba appear bright in HAADF mode, (d) X-EDS spectrum from red circle in Fig. 10(c).

X-ray photoelectron spectroscopy (XPS, PHI Quantera SXM with CasaXPS software) measurements were conducted in order to confirm the presence of Ba, Ti and O elements on the surface and investigate the nature of bonding. The peaks at binding energy of 530.0 eV and 532.0 eV indicate the presence of TiO_2 and SiO_2 bonds respectively. High resolution (slow scan) XPS confirmed the presence of BTO bonding arrangement corresponding to binding energy of 458.52 eV as shown in Fig. 10(b) by Gaussian (70%)-Lorentzian (30%) fit (using the CasaXPS software). Combining the results of TEM and XPS analysis it can be summarized that nanoNecklace comprises of BTO nanoparticles arranged along the length of large diameter SiCN-MWCNT nanotubes. The morphology of nanoNecklace can be further improved by tailoring the wetting characteristics through surface functionalization and coatings. A change in wetting characteristics will allow more uniform coverage of BTO over the MWCNT template resulting in higher dielectric surface area and hence capacitance.

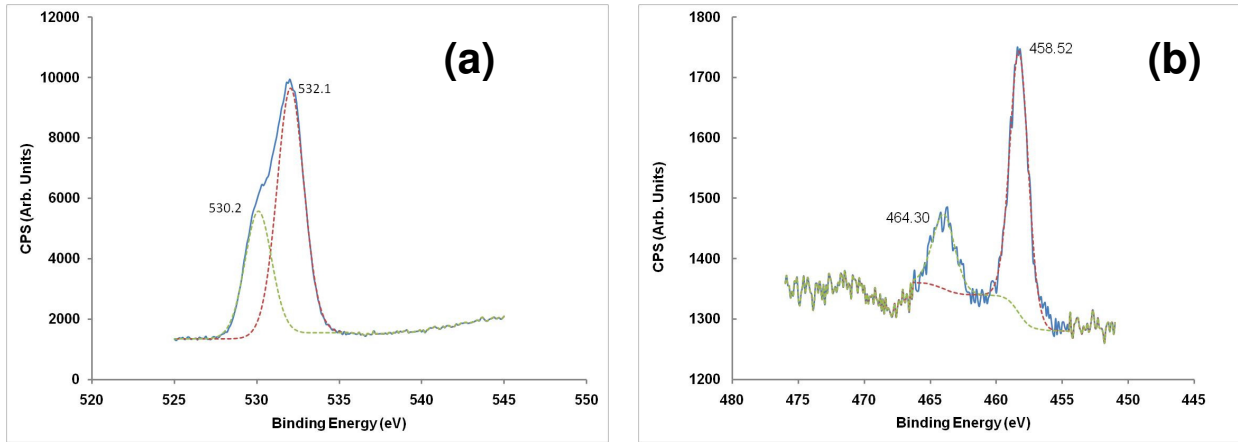


Figure 11: XPS spectra of (a) O-1s and (b) Ti-2p peaks, corresponding to BaTiO₃ and TiO₂ bonding type respectively (Dotted line is Gaussian-Lorentzian (30%) fitted XPS spectra).

The next step is to coat the BTO nanoparticles- decorated SiCN-multiwalled carbon nanotubes – “nanoNecklace” with ferrite nanoparticles and measure the magnitude of ME coupling from individual nanotubes.

(G) Magnetoelectric Gradiometer

Recently, we have reported a magnetic field sensor based on piezoelectric transformer with ring-dot electrode pattern. A piezoelectric transformer is a two port device, where on one port the applied input voltage is converted into stress through converse piezoelectric effect, and on the other port this generated stress is converted back into voltage through direct piezoelectric effect. In this prior design, a voltage was applied to the ring section at resonance frequency which induces a magnetic field in the dot section. If an external magnetic object is then brought in the vicinity of the dot section, the change in magnetic field will induce a change in the voltage gain of the transformer via the magnetoelectric (ME) effect. Here, we have combined our prior magnetic field sensor design with a new laminate geometry to achieve ME gradiometer. Our findings demonstrate enhanced sensitivity to small changes in magnetic field using the multilayer PZT ring and Terfenol-D disk. In addition, we propose a theoretical model describing the low frequency response of sensor and resonance response of the proposed ME gradiometer. A very good agreement was obtained between the experiment and theory.

Multilayer PZT disks were synthesized by tape casting technique using Ag-Pt electrodes (Dongil Tech., Korea, composition D210). The co-fired PZT element had 10-layer of 100 μm thickness with dimensions of 29 mm diameter and 1 mm thickness. Sample A was fabricated by bonding the multilayer PZT disc with co-centric Terfenol-D (diameter = 13 mm) using a Loctite E – 30CL Hysol epoxy adhesive. Curing was done in temperature range of 60 – 75 $^{\circ}\text{C}$ for one hr. Sample B (gradiometer) had ring dot electrode pattern printed on top surface of PZT (APC 841), where ring acts as the input while dot acts as the output. The output section had a diameter of 15 mm and the input section had a width of 5 mm. There was an insulation gap between input and output

section of 2 mm. The ground electrode was at the bottom of PZT. Terfenol – D disc with diameter of 13 mm was bonded on the output section as shown in Fig. 11(a) and (b).

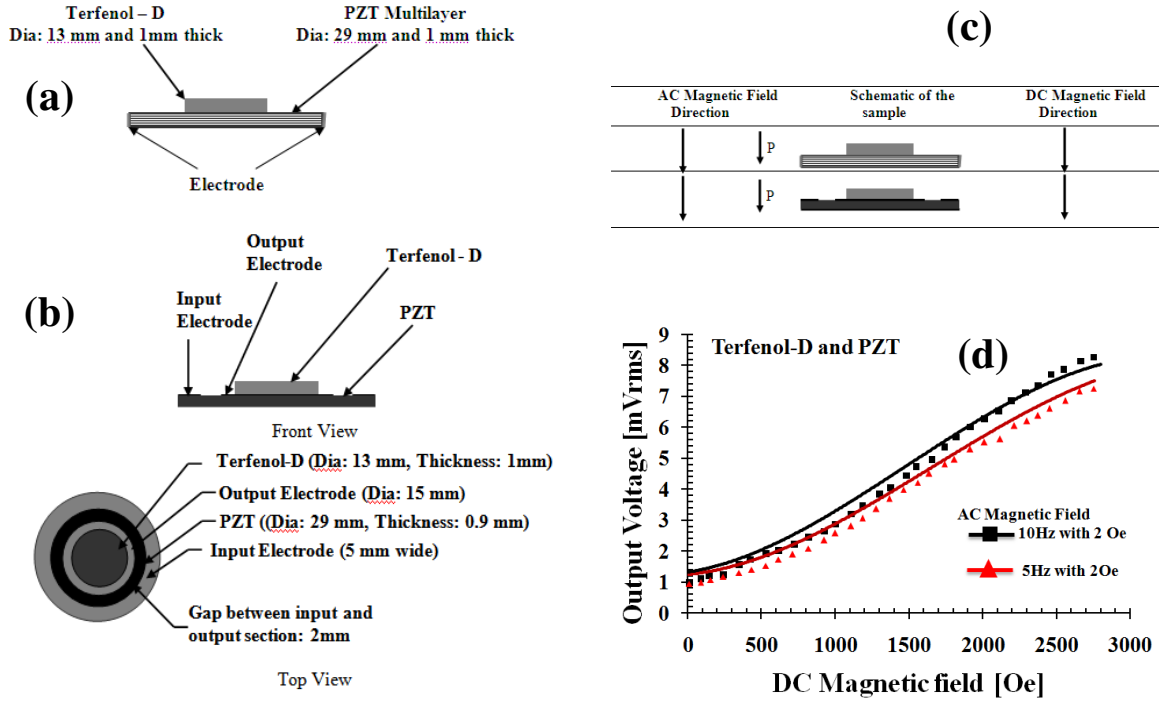


Figure 12: (a) Schematic diagram of the sensor (sample A) illustrating the dimensions and layout of various elements, (b) Schematic diagram of the ring-dot structure (sample B) illustrating the dimensions and layout of various elements. (c) AC and DC magnetic field directions used in the measurements, where P is the polarization of PZT. (d) Solid line is theoretical dependence of output voltage from the first design (multilayered PZT bonded with Terfenol-D disc, Sample A) shown in Fig. 12(a) at low frequency. Dot is output voltage at low frequency. The applied AC magnetic field was fixed at 2 Oe.

The piezoelectric constant of synthesized composite was measured by APC YE 2730A d_{33} meter. Resonance characteristics were determined by HP 4194A impedance analyzer (Hewlett Packard Co. USA). For sample A, the voltage output was measured by applying an AC magnetic field at low frequency (5 – 10 Hz) with 2Oe amplitude (H) under varying DC magnetic bias. The AC magnetic field was generated by a Helmholtz coil powered by Agilent 3320 function generator and NF high speed bipolar power amplifier (HAS 4052). DC magnetic bias was generated by using solenoid coil set powered by Kepco DC power supply. The output voltage generated from the composite was measured by using SRS DSP lock-in amplifier (model SR 830). For the gradiometer design, Sample B, an input voltage of $1 V_{p-p}$ was applied on the ring section and output voltage was measured from dot section using a Tektronix TDS 420A four channel digital oscilloscope with varying DC magnetic bias field. The frequency range was chosen near resonance frequency (90.6 kHz) of the transformer as determined from the impedance curves shown in Fig. 13. The magnetic field generated in the dot-section was measured by using the magnetic field sensor (AC/DC magnetometer from Alphalab Inc.). All the measurements were repeated to check the consistency of results.

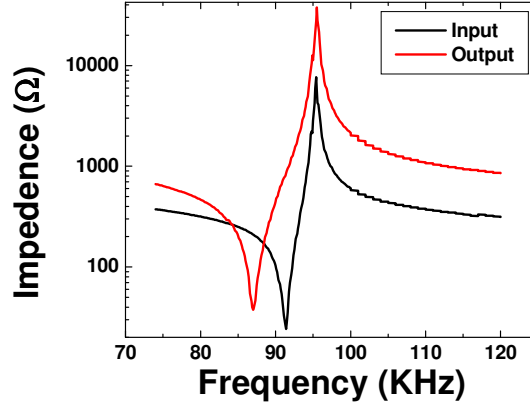


Figure 13: Impedance spectrum of the input and output section. The output was under open circuit condition when measuring the input spectrum and vice-versa.

Theory of low frequency magnetoelectric magnetic field sensor (Sample A)

Working principle of ME sensor shown in Fig. 12(a) is based on measuring the variation in ME voltage coefficient due to changes in applied magnetic field. The response of sample to the external magnetic field is related to the magnitude of ME voltage coefficient. For a given orientation of the fields as shown in Fig. 12(c), the ME voltage coefficient can be expressed as:

$$\alpha_E = 2 \frac{\mu_0 k v (1 - v) {}^p d_{31} q_{31}}{\{2 {}^p d_{31}^2 (1 - v) + {}^p \epsilon_{33} [({}^p s_{11} + {}^p s_{12})(v - 1) - v({}^m s_{11} + {}^m s_{12})]\}} \quad (1)$$

$$\times \frac{[({}^p s_{11} + {}^p s_{12})(v - 1) - k v ({}^m s_{11} + {}^m s_{12})]}{\{[\mu_0 (1 - v) - {}^m \mu_{33} v][k v ({}^m s_{12} + {}^m s_{11}) - ({}^p s_{11} + {}^p s_{12})(v - 1)] + 2 {}^m q_{31}^2 k v^2\}}$$

where $v = {}^p v / ({}^p v + {}^m v)$, k is the coupling factor, and ${}^p v$ and ${}^m v$ denote the volume of piezoelectric and magnetostrictive phase, respectively. For this case, nonzero components of ${}^p s_{ij}$, ${}^p d_{ki}$, ${}^m s_{ij}$, ${}^m q_{ki}$ are provided by Table I. Voltage output is given as: $U_{out} = \alpha_E \cdot \delta H \cdot t$, where t is the piezoelectric phase thickness. Figure 12(d) shows the theoretical and measured values of output voltage as a function of DC magnetic field, indicating very good correspondence between the model and experiment. Variation of output voltage as a function of DC magnetic field was obtained by computing the magnetic field dependence of piezomagnetic coefficient q . It can be noted from this figure that output voltage varies almost linearly with DC magnetic field at low frequencies and small AC magnetic field of 20 Oe. This linear change allows us to use this design for DC magnetic field sensing with high precision.

Table I: List of material parameters.

Piezoelectric phase	
Piezoelectric coefficients	Compliance coefficients
${}^p d_{15} = {}^p d_{24}$	${}^p s_{11} = {}^p s_{22}$
${}^p d_{31} = {}^p d_{32}$	${}^p s_{12} = {}^p s_{21}$

${}^p d_{33}$	${}^p s_{13} = {}^p s_{23} = {}^p s_{31} = {}^p s_{32}$ ${}^p s_{33}$ ${}^p s_{44} = {}^p s_{55}$ ${}^p s_{66} = 2({}^p s_{11} + {}^p s_{12})$
Magnetostrictive phase	
Piezomagnetic coefficients	Compliance coefficients
${}^m q_{15} = {}^m q_{24}$ ${}^m q_{31} = {}^m q_{32}$ ${}^m q_{33}$	${}^m s_{11} = {}^m s_{22} = {}^m s_{33}$ ${}^m s_{12} = {}^m s_{21} = {}^m s_{13} = {}^m s_{23} = {}^m s_{31}$ $= {}^m s_{32}$ ${}^m s_{44} = {}^m s_{55} = {}^m s_{66}$

Theory of magnetoelectric gradiometer (Sample B)

ME effect near electromechanical resonance (EMR) frequency for gradiometer shown in Fig.12(b) can be expressed as:

$$\alpha_E = -\frac{1}{\Delta_r} \left[\frac{2d_{31}q_{31}}{\epsilon_{33}s_{11}(1-\nu)} \left(\frac{(1+\nu)J_1(k)}{\Delta_r} - 1 \right) + \frac{\alpha_{33}}{\epsilon_{33}} \right], \quad (2)$$

where q_{ij} and d_{ij} are piezomagnetic and piezoelectric coefficients, ϵ_{ij} is the permittivity matrix, $\alpha_{33}/\epsilon_{33}$ is the value of low frequency ME coefficient. Further,

$$\Delta_r = kJ_0(k) - (1-\nu)J_1(k),$$

$$\Delta_a = 1 - K_p^2 + K_p^2(1+\nu)J_1(kR)/\Delta_r + iG, \text{ and}$$

$K_p^2 = 2d_{31}^2/\epsilon_{33}s_{11}$ is the coefficient of electromechanical coupling for radial mode, and G is the loss factor. It can be noted that the magnitude of ME effect is dependent upon the material parameter d_{31} and q_{31} .

The shift in EMR frequency range can be estimated as a function of magnetic field, H . This shift is due to change in Young's modulus (E) caused by the applied magnetic field: namely the ΔE effect. The shift δf_r in the EMR frequency range can be estimated as a function of bias magnetic field as follows:

$$\delta f_r = \frac{\Delta E f_r}{2E(1+\nu)z} \frac{(3+\nu)z^2 J_0^2(z) - 8z J_0(z) J_1(z) + [(1+\nu)z^2 + 4(1-\nu)] J_1^2(z)}{z[J_0^2(z) + J_1^2(z)] - 2J_0(z)J_1(z)}, \quad (3)$$

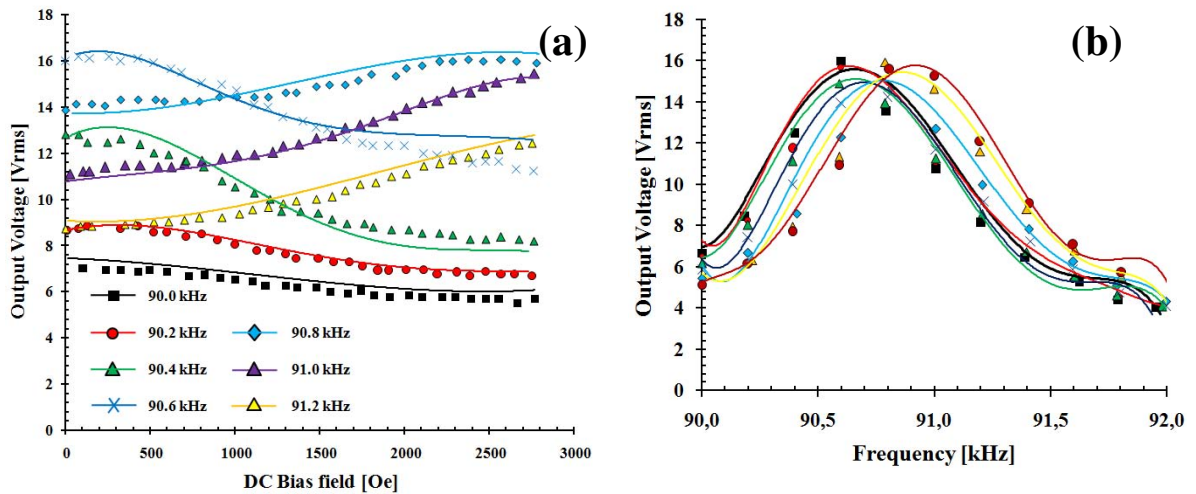
where

$$\frac{\Delta E}{E} = \frac{4}{27} E \Lambda t_2^2 \frac{[\cosh(h) - \cosh(\frac{h}{3})][\cosh(h) - 9 \cosh(\frac{h}{3})]}{[\cosh(h) + 3 \cosh(\frac{h}{3})]^2},$$

where $h = 3\chi_0 H/Ms$ is a dimensionless parameter, χ_0 is the permeability at $H=0$, $\Lambda = 3\chi/Ms^2$, and $t_2 = -B_2/2c_{44}$, Ms is the saturation magnetization, B_2 is the magnetoelastic constant, and c_{ij} is the stiffness coefficient, $z = kR$, $\nu = -s_{12}/s_{11}$ is Poisson's ratio, $k = \omega \sqrt{\rho s_{11}(1-\nu^2)}$, ρ is the density, ω is the angular frequency, and $J_0(k)$ and $J_1(k)$ are Bessel functions of the first kind. Figure 14(a) and (b) show the calculated and measured results for the gradiometer design illustrated in Fig. 12(b). These results show the variation of output voltage from the dot-section with respect to applied DC magnetic field. The measured frequency was varied in the range of EMR of the gradiometer. It can

be seen from Fig. 14(a) that there is change in slope on either side of the EMR. At the frequency of 91 and 91.2 kHz, the variation in output voltage becomes linear with increasing applied magnetic field. Figure 14(b) shows the change in amplitude of output voltage with frequency for constant applied DC magnetic field. From this figure, two regions can be clearly separated and the device can provide differential voltage as the magnetic field changes with respect to reference state as shown in Fig. 14(c).

The mechanism for large differential change can be understood by measuring the generated magnetic field in the dot section as shown in Fig. 14(d). Based on the results of this figure, the sensing mechanism can be proposed as following: A voltage is applied to the ring section at the resonance frequency which induces magnetic field in the dot section. If an external magnetic object is brought in the vicinity of the dot section than the resulting differential magnetic field will induce change in the voltage gain due to magnetoelectric effect. Figure 14(d) shows the plot of the generated AC magnetic field in the dot section as a function of frequency at constant input voltages. These measurements were in the vicinity of the EMR which is indicated by peak. It can be further seen in this figure that there is a significant change in magnitude of the generated AC magnetic field with applied input voltage to the ring section, which increases as the frequency approaches the resonance point. This generated AC magnetic field couples with the applied external magnetic field to provide differential change in the output voltage of dot section. The variation in the EMR frequency with increasing input voltage can be explained on the basis of reverse ME effect. Using the data in Fig. 14(d), we can compute the converse magnetoelectric effect (CME) of composite which is defined as change in magnetization (or in our case magnetic field) with respect to applied electric field. The CME effect is given as, $\alpha_B = (\text{dB/dV})$. At the resonance frequency, α_B can be calculated to be of the order of 3.4 G/V – 4.4 G/V. The range in the CME occurs due to the nonlinear response of the piezoelectric at higher applied voltages near resonance frequency.



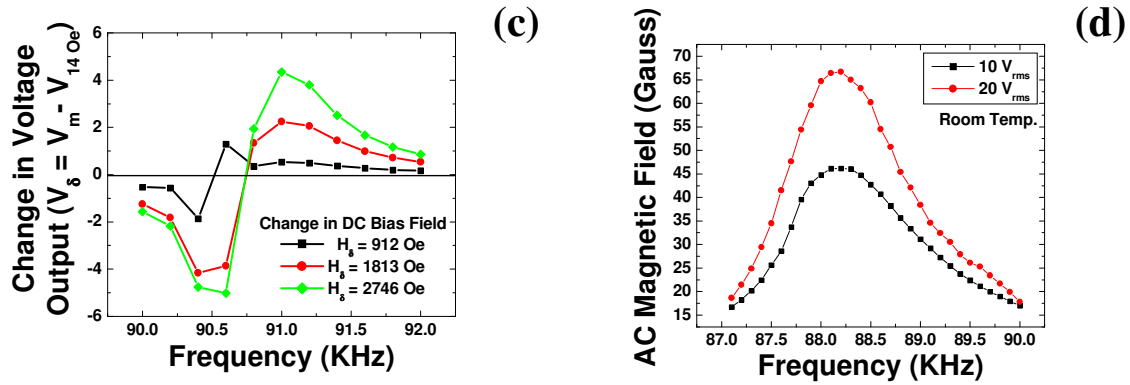


Figure 14: Sample B (a) Solid line is theoretical dependence of output voltage as a function of DC magnetic field at varying frequencies while symbols represent the experimental data, (b) Solid line is theoretical dependence of output voltage as a function of frequency at varying DC magnetic field while symbols represent the experimental data. The input voltage of gradiometer was fixed at 1V^{PP} . (c) Change in output voltage with respect to change in DC magnetic field. A linear change was observed near the resonance frequency. (d) Magnetic field generated in the dot section with applied input voltage to the ring section.

In summary, large output voltage can be obtained from Sample A at low frequencies far from EMR, thereby allowing this design to be used as a magnetic field sensor. For Sample B, there was a significant change in resonance frequency and amplitude of output voltage with applied magnetic field. The results show that magnetoelectric gradiometer or Sample B can detect changes in DC magnetic field by measuring the differential output voltage change.

Summary of the achievements: The diagram below summarizes our progress in enhancing the magnitude of ME coefficient in sintered composites. We have improved the performance by almost an order of magnitude through textured laminates.

